Eur. Phys. J. Special Topics **224**, 2867–2880 (2015)

DOI: 10.1140/epjst/e2015-02594-4

THE EUROPEAN PHYSICAL JOURNAL SPECIAL TOPICS

Regular Article

Internal resonance for nonlinear vibration energy harvesting

D.X. Cao[1,2], S. Leadenham[1], and A. Erturk[1,a]

[1] G. W. Woodruff School of Mechanical Engineering, Georgia Institute of Technology, Atlanta, GA 30332, USA
[2] College of Mechanical Engineering, Beijing Key Laboratory of Nonlinear Vibrations and Strength of Mechanical Structures, Beijing University of Technology, Beijing 100124, China

Received 21 August 2015 / Received in final form 9 September 2015
Published online 20 November 2015

Abstract. The transformation of waste vibration energy into low-power electricity has been heavily researched over the last decade to enable self-sustained wireless electronic components. Monostable and bistable nonlinear oscillators have been explored by several research groups in an effort to enhance the frequency bandwidth of operation. Linear two-degree-of-freedom (2-DOF) configurations as well as the combination of a nonlinear single-DOF harvester with a linear oscillator to constitute a nonlinear 2-DOF harvester have also been explored to develop broadband energy harvesters. In the present work, the concept of nonlinear internal resonance in a continuous frame structure is explored for broadband energy harvesting. The L-shaped beam-mass structure with quadratic nonlinearity was formerly studied in the nonlinear dynamics literature to demonstrate modal energy exchange and the saturation phenomenon when carefully tuned for two-to-one internal resonance. In the current effort, piezoelectric coupling and an electrical load are introduced, and electromechanical equations of the L-shaped energy harvester are employed to explore primary resonance behaviors around the first and the second linear natural frequencies for bandwidth enhancement. Simulations using approximate analytical frequency response equations as well as numerical solutions reveal significant bandwidth enhancement as compared to a typical linear 2-DOF counterpart. Vibration and voltage responses are explored, and the effects of various system parameters on the overall dynamics of the internal resonance-based energy harvesting system are reported.

1 Introduction

The conversion of mechanical vibration energy into low-power electricity has received growing attention as an enabling technological concept for small electronic components and wireless applications [1–5]. Various research groups have reported their

[a] e-mail: alper.erturk@me.gatech.edu

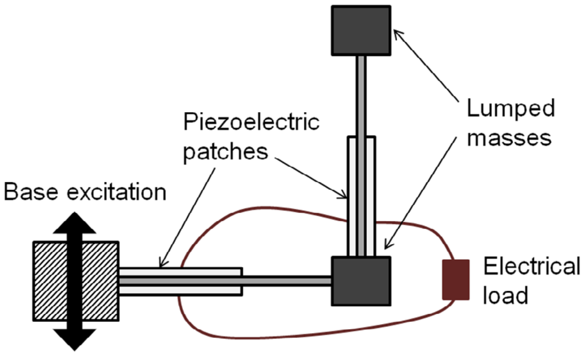

Fig. 1. Piezoelectrically coupled and electrically shunted L-shaped beam-mass structure under base excitation as a quadratically nonlinear energy harvester with two-to-one internal resonance (lumped masses are tuned to have the first two linear natural frequencies satisfy $\omega_2 \approx 2\omega_1$, while the higher natural frequencies are far removed from the first two).

work on modeling and applications of vibration-based energy harvesting using electromagnetic [6–8], electrostatic [9,10], piezoelectric [11–14] and magnetostrictive [15,16] transduction mechanisms, as well as the use of electronic and ionic electroactive polymers [17,18] and polymer electrets [19], and even flexoelectricity for energy harvesting at submicron scales [20]. Among the basic transduction mechanisms that can be used for vibration-to-electricity conversion, piezoelectric transduction has received the most attention due to the high power density and ease of application of piezoelectric materials [3,4,21].

Conventional energy harvesters [11–14] are typically designed based on the linear resonance phenomenon, and therefore they suffer from frequency bandwidth limitations and extreme sensitivity to uncertainties. In order to overcome this issue, multi-degree-of-freedom (MDOF – in simplest form 2-DOF) configurations with multiple linear resonance frequencies and designed nonlinearities with nonlinear resonances and highly inclined backbone curves have been studied for frequency bandwidth enhancement. The reader is referred to several review articles by Tang et al. [22], Pellegrini et al. [23], Twiefel and Westermann [24], Harne and Wang [25], and Daqaq et al. [26] on broadband and nonlinear energy harvesting concepts. The existing efforts on frequency bandwidth enhancement in vibration energy harvesters range from 2-DOF linear concepts [27–31] to monostable [32–34] and bistable [35–41] single-DOF energy harvesters, as well as 2-DOF combination of linear and nonlinear oscillators [42,43].

The present work is focused on the exploitation of two-to-one internal resonance in the L-shaped beam-mass structure of Haddow et al. [44] (as a simple alternative to the recently explored snap-through configuration with internal resonance by Chen and Jiang [45]). Linearized distributed-parameter electroelastic dynamics of an L-shaped piezoelectric energy harvester was formerly described by Erturk et al. [46]. Therefore the present work is centered on the nonlinear problem for the exploitation of two-to-one internal resonance with a focus on the two primary resonance cases for excitations near the first two natural frequencies. In the following, the governing nonlinear electromechanical equations are analyzed using the method of multiple scales for the modal mechanical response amplitudes and the voltage output across the electrical load. The effects of various system parameters on the electromechanical frequency response are then reported, and bandwidth enhancement is discussed. Comparisons of the perturbation-based approximate analytical solution with time-domain exact numerical simulations are also given briefly.

2 Governing electromechanical equations and perturbation analysis

2.1 Governing equations

Linearized two-way electromechanical coupling of piezoelectricity [21] and a resistive electrical load are introduced to the governing equations of the L-shaped passive beam-mass structure[1] [44] to yield the following dimensionless mechanical force balance and electrical current balance equations:

$$\begin{aligned}
&\begin{bmatrix} \ddot{u}_1 \\ \ddot{u}_2 \end{bmatrix} + 2\varepsilon \begin{bmatrix} \mu_1 & 0 \\ 0 & \mu_2 \end{bmatrix} \begin{Bmatrix} \dot{u}_1 \\ \dot{u}_2 \end{Bmatrix} + \begin{bmatrix} \omega_1^2 & 0 \\ 0 & \omega_2^2 \end{bmatrix} \begin{Bmatrix} u_1 \\ u_2 \end{Bmatrix} - \varepsilon \begin{Bmatrix} \theta_1 \\ \theta_2 \end{Bmatrix} v \\
&\quad +\varepsilon \begin{bmatrix} X_{11} & X_{12} & X_{13} \\ X_{21} & X_{22} & X_{23} \end{bmatrix} \begin{Bmatrix} (\dot{u}_1)^2 \\ \dot{u}_1 \dot{u}_2 \\ (\dot{u}_2)^2 \end{Bmatrix} + \varepsilon \begin{bmatrix} Y_{11} & Y_{12} & Y_{13} & Y_{14} \\ Y_{21} & Y_{22} & Y_{23} & Y_{24} \end{bmatrix} \begin{Bmatrix} u_1 \ddot{u}_1 \\ u_1 \ddot{u}_2 \\ u_2 \ddot{u}_1 \\ u_2 \ddot{u}_2 \end{Bmatrix} \\
&\quad +2\varepsilon F \Omega \cos(\Omega t) \begin{bmatrix} Z_{11} & Z_{12} \\ Z_{21} & Z_{22} \end{bmatrix} \begin{Bmatrix} u_1 \\ u_2 \end{Bmatrix} = 2F \begin{Bmatrix} K_1 \\ K_2 \end{Bmatrix} \cos \Omega t \\
&\dot{v} + \lambda v + \kappa_1 \dot{u}_1 + \kappa_2 \dot{u}_2 = 0
\end{aligned} \tag{1}$$

where u_i $(i = 1, 2)$ are the modal displacements that are of order unity, θ_i are the piezoelectric coupling terms in the mechanical equations, κ_i are the piezoelectric coupling terms in the electrical circuit equation, λ is the reciprocal of the time constant of the resistive-capacitive circuit (due to the external resistive load and internal piezoelectric capacitance), μ_i is mechanical damping term under short-circuit conditions, Ω is the frequency of the base excitation force F, and ε is a small bookkeeping parameter, while the remaining terms (ω_i, X_{ij}, Y_{ij}, Z_{ij}, K_i) can be found in Ref. [44]. Furthermore, the modal displacements u_1 and u_2 can be combined with the structural linear eigenfunctions to approximate the vibration response of the structure as in Haddow et al. [44].

2.2 Method of multiple scales

The method of multiple scales [47] is employed to obtain an approximate solution for the electromechanical response in the form of

$$\begin{aligned}
u_i\,(t;\varepsilon) &= u_{i0}(T_0, T_1) + \varepsilon u_{i1}(T_0, T_1) \\
v\,(t;\varepsilon) &= u_{30}(T_0, T_1) + \varepsilon u_{31}(T_0, T_1)
\end{aligned} \tag{2}$$

where $T_0 = t$ and $T_1 = \varepsilon t$ are the time scales. The derivatives with respect to time are also expansions as partial derivatives with respect to these time scales:

$$\frac{d}{dt}(\cdot) = (D_0 + \varepsilon D_1)(\cdot), \quad \frac{d^2}{dt^2}(\cdot) = (D_0^2 + 2\varepsilon D_0 D_1)(\cdot) \tag{3a}$$

[1] The reader is referred to Haddow et al. [44] for derivation and non-dimensionalization of the passive 2-DOF structural equations, while Erturk et al. [46] is a useful reference for linearized distributed-parameter electroelastic formulation of the L-shaped structure (in terms of introducing the piezoelectric effect and electrical load to the L-shaped beam-mass structure).

$$D_0 \equiv \frac{\partial}{\partial T_0}, \quad D_1 \equiv \frac{\partial}{\partial T_1} \tag{3b}$$

where terms of order ε^2 have been neglected.

Soft excitation is assumed as common practice in primary resonance analysis so that

$$F = \varepsilon f. \tag{4}$$

Substituting Eqs. (2)–(4) into (1) and equating coefficients of like powers of ε gives the following equations for orders ε^0 and ε^1:

$$\begin{aligned} &D_0^2 u_{i0} + \omega_i^2 u_{i0} = 0 \\ &D_0 u_{30} + \lambda u_{30} = -\kappa_1 D_0 u_{10} - \kappa_2 D_0 u_{20} \end{aligned} \tag{5}$$

$$\begin{aligned} D_0^2 u_{i1} + \omega_1^2 u_{i1} &= -2D_0 D_1 u_{i0} - 2\mu_i D_0 u_{i0} + \theta_i u_{30} - X_{i1}\left(D_0 u_{10}\right)^2 - Y_{i1} u_{10}(D_0^2 u_{10}) \\ &\quad - Y_{i2} u_{10}(D_0^2 u_{20}) - X_{i2}(D_0 u_{10})(D_0 u_{20}) - Y_{i3} u_{20}(D_0^2 u_{10}) \\ &\quad - X_{i3}\left(D_0 u_{20}\right)^2 - Y_{i4} u_{20}(D_0^2 u_{20}) + 2fK_1 \cos(\Omega T_0) \\ D_1 u_{31} + \lambda u_{31} &= -D_0 u_{30} - \kappa_1 (D_0 u_{11} + D_1 u_{10}) - \kappa_2 (D_0 u_{21} + D_1 u_{20}) \end{aligned} \tag{6}$$

From Eq. (5),

$$u_{i0} = A_i\left(T_1\right) \mathrm{e}^{i\omega_i T_0} + cc \tag{7a}$$

$$\begin{aligned} u_{30} &= B(T_1)\mathrm{e}^{-\lambda T_0} + B_1\left(T_1\right)\mathrm{e}^{i\omega_1 T_0} + B_2\left(T_1\right)\mathrm{e}^{i\omega_2 T_0} + cc \\ &= B(T_1)\mathrm{e}^{-\lambda T_0} - \frac{i\kappa_1\omega_1 A_1\left(T_1\right)\mathrm{e}^{i\omega_1 T_0}}{\lambda + i\omega_1} - \frac{i\omega_2\kappa_2 A_2\left(T_1\right)\mathrm{e}^{i\omega_2 T_0}}{\lambda + i\omega_2} + cc \end{aligned} \tag{7b}$$

where $A_i(T_1)$ and $B(T_1)$ are unknown functions at this point and cc stands for the complex conjugate of the preceding terms.

Substituting Eqs. (7) into (6) leads to

$$\begin{aligned} D_0^2 u_{11} + \omega_1^2 u_{11} = &-i\omega_1\left(2D_1 A_1 + 2\mu_1 A_1 + \frac{\theta_1\kappa_1 A_1}{i\omega_1 + \lambda}\right)\mathrm{e}^{i\omega_1 T_0} - \frac{i\omega_2\theta_1\kappa_2 A_2 \mathrm{e}^{i\omega_2 T_0}}{i\omega_2 + \lambda} \\ &+ \omega_1^2\left(X_{11} + Y_{11}\right)A_1^2\mathrm{e}^{2i\omega_1 T_0} + \omega_2^2\left(X_{13} + Y_{14}\right)A_2^2\mathrm{e}^{2i\omega_2 T_0} \\ &+ \left(Y_{12}\omega_2^2 + X_{12}\omega_1\omega_2 + Y_{13}\omega_1^2\right)A_2 A_1 \mathrm{e}^{i(\omega_1+\omega_2)T_0} \\ &+ \left(Y_{12}\omega_2^2 - X_{12}\omega_1\omega_2 + Y_{13}\omega_1^2\right)A_2\overline{A_1}\mathrm{e}^{i(\omega_2-\omega_1)T_0} \\ &+ 2\omega_1^2(Y_{11} - X_{11})A_1\overline{A_1} + 2\omega_2^2(Y_{14} - X_{13})A_2\overline{A_2} + 2fK_1\cos(\Omega T_0) + cc \end{aligned} \tag{8a}$$

$$\begin{aligned} D_0^2 u_{21} + \omega_2^2 u_{21} = &-i\omega_2\left(2D_1 A_2 + 2\mu_2 A_2 + \frac{\theta_2\kappa_2 A_2}{i\omega_2 + \lambda}\right)\mathrm{e}^{i\omega_2 T_0} - \frac{i\omega_1\theta_2\kappa_1 A_1 \mathrm{e}^{i\omega_1 T_0}}{i\omega_1 + \lambda} \\ &+ \omega_1^2\left(X_{21} + Y_{21}\right)A_1^2\mathrm{e}^{2i\omega_1 T_0} + \omega_2^2\left(X_{23} + Y_{24}\right)A_2^2\mathrm{e}^{2i\omega_2 T_0} \\ &+ \left(Y_{22}\omega_2^2 + X_{22}\omega_1\omega_2 + Y_{23}\omega_1^2\right)A_1 A_2 \mathrm{e}^{i(\omega_1+\omega_2)T_0} \\ &+ \left(Y_{22}\omega_2^2 - X_{22}\omega_1\omega_2 + Y_{23}\omega_1^2\right)A_2\overline{A_1}\mathrm{e}^{i(\omega_2-\omega_1)T_0} \\ &+ 2\omega_1^2(Y_{21} - X_{21})A_1\overline{A_1} + 2\omega_2^2(Y_{24} - X_{23})A_2\overline{A_2} + 2fK_2\cos(\Omega T_0) + cc \end{aligned} \tag{8b}$$

where $\bar{A}_i$ is the complex conjugate of A_i. Note that the A_i terms are chosen to eliminate the secular terms in the time scale T_0 from u_{11} and u_{21} [44]. Therefore the A_i terms depend on the relationships among the excitation frequency and the linear natural frequencies. The excitation cases of Ω near ω_1 and Ω near ω_2 (for ω_2 near $2\omega_1$) are discussed next to obtain the frequency response equations.

3 Frequency response equations and results for the primary resonance $\Omega \approx \omega_1$

3.1 Approximate analytical expressions

Two detuning parameters, σ_1 (internal detuning parameter) and σ_2 (external detuning parameter), are introduced to describe the proximity of ω_2 to $2\omega_1$ and Ω to ω_1, respectively. Therefore the frequency relations for the two-to-one internal resonance and the first primary resonance of $\Omega \approx \omega_1$ are

$$\omega_2 = 2\omega_1 + \varepsilon\sigma_1, \quad \Omega = \omega_1 + \varepsilon\sigma_2. \tag{9}$$

In view of Eq. (8), the secular terms in the time scale T_0 can then be eliminated from u_{11} and u_{21} provided that

$$\begin{aligned} &2i\left[(D_1A_1 + \mu_1A_1) + \rho_1(\lambda - i\omega_1)A_1\right] - 4C_1A_2\overline{A_1}\mathrm{e}^{i\sigma_1T_1} - \frac{(2fK_1)}{\omega_1}\mathrm{e}^{i\sigma_2T_1} = 0 \\ &2i\left[(D_1A_2 + \mu_2A_2) + \rho_2(\lambda - i\omega_2)A_2\right] - 4C_2A_1^2\mathrm{e}^{-i\sigma_1T_1} = 0 \end{aligned} \tag{10}$$

where

$$\begin{aligned} &C_1 = \frac{Y_{12}\omega_2^2 - X_{12}\omega_1\omega_2 + Y_{13}\omega_1^2}{4\omega_1}, \quad C_2 = \frac{\omega_1^2\,(X_{21} + Y_{21})}{4\omega_2} \\ &\rho_1 = \frac{\theta_1\kappa_1}{2(\lambda^2 + \omega_1^2)}, \quad \rho_2 = \frac{\theta_2\kappa_2}{2(\lambda^2 + \omega_2^2)}. \end{aligned} \tag{11}$$

The unknowns A_i can be expressed in polar form as

$$A_1 = \frac{1}{2\sqrt{C_1C_2}}a_1\mathrm{e}^{i\beta_1}, \qquad A_2 = \frac{1}{2C_1}a_2\mathrm{e}^{i\beta_2}, \tag{12}$$

where the a_i and β_i terms are real functions of the time scale T_1. After substituting Eq. (12) into Eq. (10) and then separating the result into real and imaginary parts, one can obtain

$$\begin{aligned} &a_1' + (\mu_1 + \rho_1\lambda)a_1 - a_2a_1\sin\gamma_1 - F\sin\gamma_2 = 0, \\ &a_1\beta_1' - \rho_1a_1\omega_1 + a_2a_1\cos\gamma_1 + F\cos\gamma_2 = 0, \\ &a_2' + (\mu_2 + \rho_2\lambda)a_2 + a_1^2\sin\gamma_1 = 0, \\ &a_2\beta_2' - \rho_2a_2\omega_2 + a_1^2\cos\gamma_1 = 0, \end{aligned} \tag{13}$$

which are the electromechanical modulation equations (where the prime denotes differentiation with respect to T_1) and

$$F = \frac{2K_1\sqrt{C_1C_2}f}{\omega_1}, \quad \gamma_1 = \sigma_1T_1 - 2\beta_1 + \beta_2, \quad \gamma_2 = \sigma_2T_1 - \beta_1 \tag{14}$$

Steady-state response implies $a_1' = a_2' = 0$ and $\gamma_1' = \gamma_2' = 0$, one can then find $\beta_1' = \sigma_2$ and $\beta_2' = 2\sigma_2 - \sigma_1$, yielding

$$\begin{aligned}
&(\rho_1\lambda + \mu_1)\, a_1 - a_2 a_1 \sin\gamma_1 - F\sin\gamma_2 = 0,\\
&\rho_1 a_1\omega_1 - \sigma_2 a_1 - a_2 a_1 \cos\gamma_1 - F\cos\gamma_2 = 0,\\
&(\rho_2\lambda + \mu_2)\, a_2 + a_1^2 \sin\gamma_1 = 0\\
&\rho_2\omega_2 a_2 - (2\sigma_2 - \sigma_1)a_2 - a_1^2\cos\gamma_1 = 0
\end{aligned} \tag{15}$$

and

$$a_2 = \frac{a_1^2}{\left\{\Gamma_1^2 + \Gamma_4^2\right\}^{1/2}}, \tag{16a}$$

$$a_1^6 + 2\left[\Gamma_1\Gamma_2 + \Gamma_3\Gamma_4\right] a_1^4 + \left[\Gamma_1^2 + \Gamma_4^2\right]\left[\left(\Gamma_2^2 + \Gamma_3^2\right) a_1^2 - F^2\right] = 0, \tag{16b}$$

where

$$\begin{aligned}
&\Gamma_1 = \sigma_1 - 2\sigma_2 + \rho_2\omega_2 \quad \Gamma_2 = \sigma_2 - \rho_1\omega_1\\
&\Gamma_3 = \mu_1 + \rho_1\lambda \quad \Gamma_4 = \mu_2 + \rho_2\lambda.
\end{aligned} \tag{17}$$

At steady state, the homogeneous part of Eq. (7b) vanishes (i.e. $B(T_1) \to 0$ as $T_0 = t \to \infty$ since $B(T_1)$ is bounded and $\lambda > 0$), yielding the following expression for the steady-state complex voltage amplitudes in terms of the vibration amplitudes

$$\begin{aligned}
\frac{B_1}{A_1} &= -\frac{i\kappa_1\omega_1}{\lambda + i\omega_1} \to -\frac{i\kappa_1\Omega}{\lambda + i\Omega}\\
\frac{B_2}{A_2} &= -\frac{i\kappa_2\omega_2}{\lambda + i\omega_2} \to -\frac{2i\kappa_2\Omega}{\lambda + 2i\Omega}.
\end{aligned} \tag{18}$$

Therefore, at steady state

$$\begin{aligned}
u_{10} &= \frac{a_1}{\sqrt{C_1 C_2}}\cos(\Omega t - \gamma_2)\\
u_{20} &= \frac{a_2}{C_1}\cos(2\Omega t + \gamma_1 - \gamma_2)\\
u_{30} &= \frac{\kappa_1\Omega}{\sqrt{\lambda^2 + \Omega^2}}\frac{a_1}{\sqrt{C_1C_2}}\cos(\Omega t - \gamma_2 + \psi_1) + \frac{2\kappa_2\Omega}{\sqrt{\lambda^2 + 4\Omega^2}}\frac{a_2}{C_1}\cos(2\Omega t + \gamma_1 - \gamma_2 + \psi_2)
\end{aligned} \tag{19}$$

where ψ_1 and ψ_2 are the arguments of B_1/A_1 and B_2/A_2, respectively. Since the voltage response contains both frequency components, the root-mean-square (RMS) voltage across the load is:

$$v_{RMS} = \frac{1}{\sqrt{2}}\sqrt{\frac{(a_1\kappa_1\Omega)^2}{C_1C_2\left(\lambda^2 + \Omega^2\right)} + \frac{4\left(a_2\kappa_2\Omega\right)^2}{C_1^2\left(\lambda^2 + 4\Omega^2\right)}}. \tag{20}$$

3.2 Results and discussion

Approximate analytical results are demonstrated for the nonlinear electromechanical frequency response equations, and the effects of various system parameters are discussed next. The parameters ω_i, X_{ij}, Y_{ij}, X_{ij}, K_i are chosen as in Ref. [44], while the other parameters are $\mu_1 = 0.001$, $\mu_2 = 0.005$, $\lambda = 5$, $\kappa_1 = 0.5$, $\kappa_2 = 0.5$, $\theta_1 = 2$,

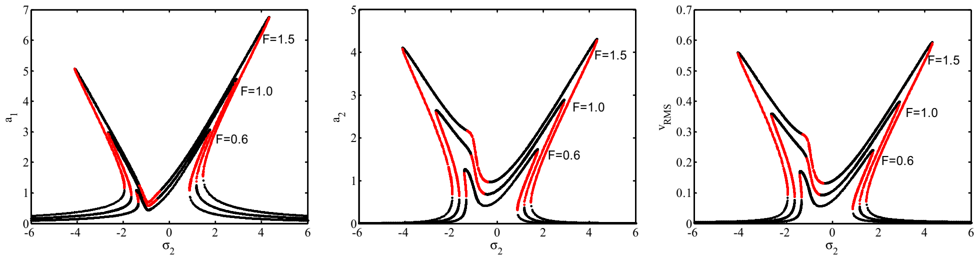

Fig. 2. Modal vibration and voltage output frequency response curves versus external detuning parameter σ_2 for different excitation levels ($F = 0.6, 1.0, 1.5$) and $\Omega \approx \omega_1$. Black curves are stable and red curves are unstable solutions.

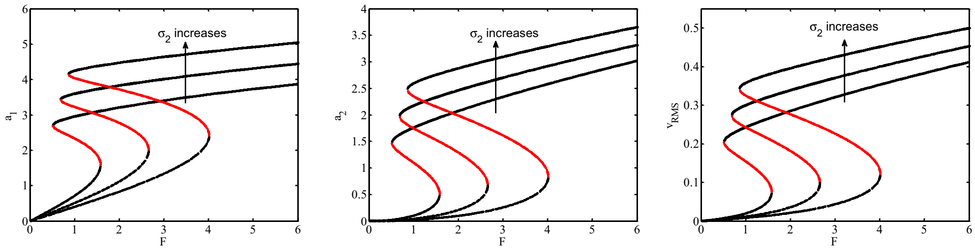

Fig. 3. Modal vibration amplitudes and voltage output versus excitation amplitude F for different values of external detuning parameter ($\sigma_2 = 1.5, 2.0, 2.5$) and $\Omega \approx \omega_1$. Black curves are stable and red curves are unstable solutions.

$\theta_2 = 5$, and $\sigma_1 = -2$. In Fig. 2, the modal vibration and voltage frequency response curves are shown as functions of the external detuning parameter σ_2 for different excitation amplitude levels. There are regions where the solution is multi-valued and there exist double jump for up and down sweeps at the edges of these regions. As the excitation level increases, a high energy attractor develops and grows over a broad range of frequencies, yielding broadband energy harvesting capabilities. In Fig. 3, the modal vibration and voltage outputs (both stable and unstable solutions) are plotted as functions of the excitation level (F) for different external detuning values. Once again, there exist regions of forcing where the electromechanical response is multi-valued.

Mechanical damping is an important parameter for the nonlinear energy harvesting system (as damping typically affects the performance of nonlinear vibrating systems). The modal vibration and voltage frequency response curves for different values of damping ratio (μ_2 for mode 2 is chosen here) are plotted in Fig. 4. The effect of the nonlinearity is more pronounced with reduced mechanical damping. The peak response amplitude and the bandwidth of frequency responses increase as mechanical damping is decreased. Therefore, low mechanical damping (i.e. high mechanical quality factor) is preferred for both increased electrical output and bandwidth.

In the governing equations, the product of piezoelectric capacitance and external load resistance is embedded in the single term λ, which is the reciprocal of the time constant for the resistive-capacitive circuit. This term (λ) is therefore inversely proportional to the external load resistance. That is, the short-circuit and the open-circuit conditions are $\lambda \to \infty$ and $\lambda \to 0$, respectively. In Fig. 5, the modal vibration and voltage frequency response curves are displayed for different λ values. Certain values of λ result in significant shortening in the bandwidth of the nonlinear frequency

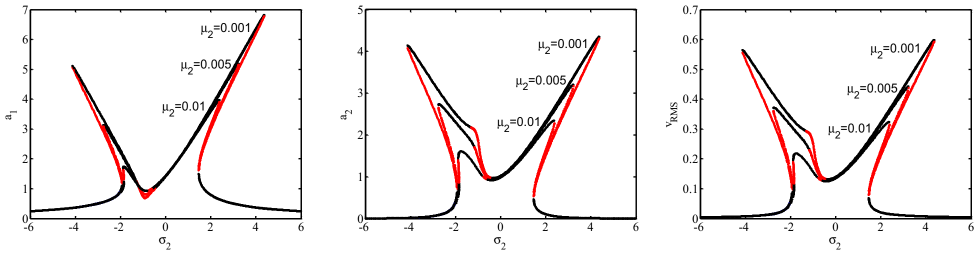

Fig. 4. Modal vibration and voltage output frequency response curves versus external detuning parameter σ_2 for different damping ratios ($\mu_2 = 0.001,\ 0.005,\ 0.01$) and $\Omega \approx \omega_1$. Black curves are stable and red curves are unstable solutions.

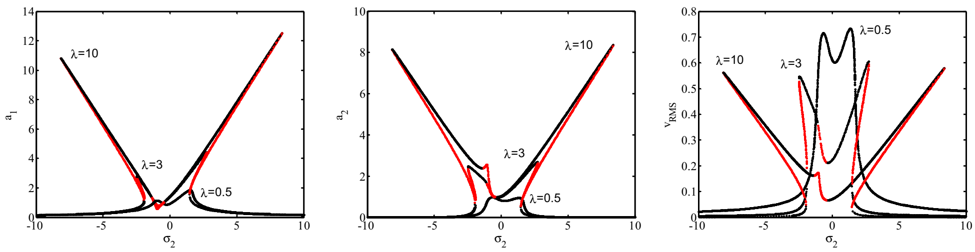

Fig. 5. Modal vibration and voltage output frequency response curves versus external detuning parameter σ_2 for different values of the reciprocal of time constant ($\lambda = 0.5, 3, 10$) and $\Omega \approx \omega_1$. Black curves are stable and red curves are unstable solutions.

response curves as a result of dissipation due to Joule heating in the resistor [21] as demonstrated previously by Leadenham and Erturk [48].

4 Frequency response equations and results for the primary resonance $\Omega \approx \omega_2$

4.1 Approximate analytical expressions

For the second primary resonance case, $\Omega \approx \omega_2$, the frequency relations are

$$\omega_2 = 2\omega_1 + \varepsilon\sigma_1, \quad \Omega = \omega_2 + \varepsilon\sigma_2 \tag{21}$$

where the internal detuning parameter σ_1 (for two-to-one internal resonance) is as previously defined, while the external detuning parameter σ_2 has been redefined.

Based on Eq. (8), the secular terms in the time scale T_0 are then eliminated from u_{11} and u_{21} when the following equations are satisfied:

$$\begin{aligned} &2i\left[(D_1A_1 + \mu_1A_1) + \rho_1(\lambda - i\omega_1)A_1\right] - 4C_1A_2\overline{A_1}\mathrm{e}^{i\sigma_1T_1} = 0 \\ &2i\left[(D_1A_2 + \mu_2A_2) + \rho_2(\lambda - i\omega_2)A_2\right] - 4C_2A_1^2\mathrm{e}^{-i\sigma_1T_1} - \frac{(2fK_1)}{\omega_2}\mathrm{e}^{i\sigma_2T_1} = 0 \end{aligned} \tag{22}$$

where C_1, C_2 and ρ_1, ρ_2 are defined in Eq. (11).

In order to solve for A_i in Eq. (22), it is convenient to use the polar forms given in Eq. (12). Substituting Eq. (12) into (22) and separating the result into real and imaginary parts, one can obtain

$$
\begin{aligned}
&a_1' + (\mu_1 + \rho_1\lambda)a_1 - a_2 a_1 \sin\gamma_1 = 0\\
&a_1\beta_1' - \rho_1 a_1\omega_1 + a_2 a_1 \cos\gamma_1 = 0\\
&a_2' + (\mu_2 + \rho_2\lambda)a_2 + a_1^2 \sin\gamma_1 - F\sin\gamma_2 = 0\\
&a_2\beta_2' - \rho_2\omega_2 a_2 + a_1^2\cos\gamma_1 + F\cos\gamma_2 = 0
\end{aligned}
\tag{23}
$$

where F is now defined as

$$
F = \frac{2C_1K_2f}{\omega_2}, \quad \gamma_1 = \sigma_1 T_1 - 2\beta_1 + \beta_2, \quad \gamma_2 = \sigma_2 T_1 - \beta_2. \tag{24}
$$

At steady state, $a_1' = a_2' = 0$ and $\gamma_1' = \gamma_2' = 0$, yielding $\beta_2' = \sigma_2$ and $\beta_1' = (\sigma_1 + \sigma_2)/2$. One can then rewrite Eq. (23) as

$$
\begin{aligned}
&\left[(\mu_1 + \rho_1\lambda) - a_2\sin\gamma_1\right] a_1 = 0\\
&\left[\frac{1}{2}(\sigma_1 + \sigma_2) - \rho_1\omega_1 + a_2\cos\gamma_1\right] a_1 = 0\\
&(\mu_2 + \rho_2\lambda)a_2 + a_1^2\sin\gamma_1 - F\sin\gamma_2 = 0\\
&(\sigma_2 - \rho_2\omega_2)a_2 + a_1^2\cos\gamma_1 + F\cos\gamma_2 = 0.
\end{aligned}
\tag{25}
$$

Following Haddow et al. [44], there are two possible solutions:

$$
a_1 = 0, \quad a_2 = \frac{F}{\sqrt{(\mu_2 + \rho_2\lambda)^2 + (\sigma_2 - \rho_2\omega_2)^2}} \tag{26a}
$$

$$
\tan\gamma_2 = \frac{\mu_2 + \rho_2\lambda}{\rho_2\omega_2 - \sigma_2}, \text{and } \gamma_1 \text{ is indeterminate;} \tag{26b}
$$

and

$$
a_1^2 = (\Gamma_1\Gamma_2 - \Gamma_3\Gamma_4) \pm \sqrt{F^2 - (\Gamma_1\Gamma_4 + \Gamma_2\Gamma_3)^2} \tag{27a}
$$

$$
a_2 = \sqrt{(\mu_1 + \rho_1\lambda)^2 + \left[\frac{1}{2}(\sigma_1 + \sigma_2) - \rho_1\omega_1\right]^2} \tag{27b}
$$

where

$$
\Gamma_1 = \frac{1}{2}(\sigma_2 + \sigma_1) - \rho_1\omega_1, \quad \Gamma_2 = \sigma_2 - \rho_2\omega_2, \quad \Gamma_3 = \mu_1 + \rho_1\lambda, \quad \Gamma_4 = \mu_2 + \rho_2\lambda \tag{28a}
$$

$$
\tan\gamma_1 = \frac{-2(\mu_1 + \rho_1\lambda)}{2\rho_1\omega_1 - (\sigma_1 + \sigma_2)}, \quad \tan\gamma_2 = \frac{\Gamma_3 a_1^2 + \Gamma_4 a_2^2}{\Gamma_1 a_1^2 - \Gamma_2 a_2^2}. \tag{28b}
$$

The first possibility is the approximate solution of the linear problem, which could also be deduced from Eq. (8) if ω_2 had been far removed from $2\omega_1$; i.e. the case of no internal resonance. The second possibility results in the so-called saturation phenomenon [44,49,50]; i.e. in this latter case, the amplitude (a_2) of the directly excited mode is independent of the amplitude of the excitation, whereas the amplitude (a_1) of the mode that is not directly excited does depend on the amplitude of the excitation.

The second solution may take place for $\Gamma_1\Gamma_2 - \Gamma_3\Gamma_4 \leq 0$ and $\Gamma_1\Gamma_2 - \Gamma_3\Gamma_4 > 0$ [44]. These cases can be considered separately in the following analysis: Case (1) is $\Gamma_1\Gamma_2 - \Gamma_3\Gamma_4 \leq 0$, a single real root for exists if $F \geq F_2 = \sqrt{(\Gamma_1^2 + \Gamma_3^2)(\Gamma_2^2 + \Gamma_4^2)}$ and if $F < F_2$, no real root exists; Case (2) is $\Gamma_1\Gamma_2 - \Gamma_3\Gamma_4 > 0$, two real roots for a_1 exist if $F_2 > F > F_1 = |\Gamma_1\Gamma_4 + \Gamma_2\Gamma_3|$, and one real root exists if $F > F_2$, and no real root exists if $F < F_1$. Substituting F_2 from Case (1) into Eq. (26a), the solution of the linearized system, one can find that a_2 in Eq. (26a) is the same as that given by Eq. (27b), the saturation value. In other words, when F is small, the solution is that of the linearized set of equations.

As done previously with Eq. (18), the complex voltage amplitudes can be written in terms of the vibration amplitudes. Therefore, at steady state

$$\begin{aligned}
u_{10} &= 0 \\
u_{20} &= \frac{a_2}{C_1}\cos(\Omega t - \gamma_2) \\
u_{30} &= \frac{\kappa_2\Omega}{\sqrt{\lambda^2+\Omega^2}}\frac{a_2}{C_1}\cos(\Omega t - \gamma_2 + \psi_2)
\end{aligned} \tag{29}$$

with the RMS voltage output

$$v_{RMS} = \frac{1}{\sqrt{2}}\frac{a_2\kappa_2\Omega}{C_1\sqrt{\lambda^2+\Omega^2}} \tag{30}$$

or

$$\begin{aligned}
u_{10} &= \frac{a_1}{\sqrt{C_1C_2}}\cos\left(\frac{1}{2}\Omega t - \frac{\gamma_1+\gamma_2}{2}\right) \\
u_{20} &= \frac{a_2}{C_1}\cos(\Omega t - \gamma_2) \\
u_{30} &= \frac{\kappa_1\Omega}{\sqrt{4\lambda^2+\Omega^2}}\frac{a_1}{\sqrt{C_1C_2}}\cos\left(\frac{1}{2}\Omega t - \frac{\gamma_1+\gamma_2}{2} + \psi_1\right) \\
&\quad + \frac{\kappa_2\Omega}{\sqrt{\lambda^2+\Omega^2}}\frac{a_2}{C_1}\cos(\Omega t - \gamma_2 + \psi_2)
\end{aligned} \tag{31}$$

with the RMS voltage output

$$v_{RMS} = \frac{1}{\sqrt{2}}\sqrt{\frac{(a_1\kappa_1\Omega)^2}{C_1C_2(4\lambda^2+\Omega^2)} + \frac{(a_2\kappa_2\Omega)^2}{C_1^2(\lambda^2+\Omega^2)}} \tag{32}$$

where ψ_1 and ψ_2 are the arguments of B_1/A_1 and B_2/A_2 in Eq. (18).

4.2 Results and discussion

Figure 6 illustrates the modal vibration and voltage output curves versus excitation level for different values of external detuning parameter (while the internal detuning parameter is the same as before, $\sigma_1 = -2$). Here, $\sigma_2 = 2$ corresponds to $\Gamma_1\Gamma_2 - \Gamma_3\Gamma_4 \leq 0$, while $\sigma_2 = 3$ and $\sigma_2 = 4$ correspond to $\Gamma_1\Gamma_2 - \Gamma_3\Gamma_4 > 0$. Both stable and unstable solutions are shown (in black and red colors, respectively). In case of $\sigma_2 = 2$, when $F \leq F_2$, the only solution is due to Eq. (26). For $F > F_2$, the second solution given by Eq. (27), is also possible. For $\sigma_2 = 3$ and $\sigma_2 = 4$, when $F \leq F_1$, the only solution is given by Eq. (26). For $F_2 > F > F_1$, there are three possible values of a_1 (one due to Eq. (26) and two due to Eq. (27)) and two values of a_2. At the edges of the

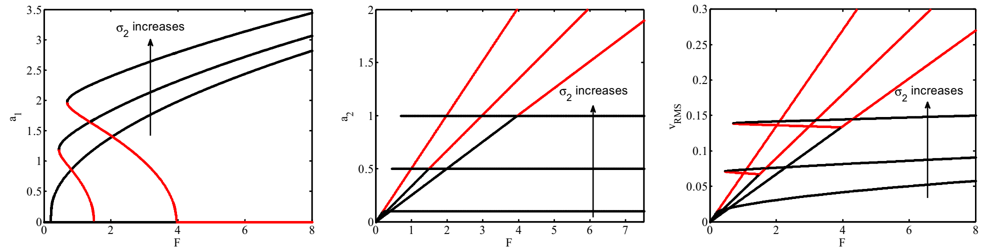

Fig. 6. Modal vibration amplitudes and RMS voltage output versus excitation amplitude F for different values of external detuning parameter ($\sigma_2 = 2, 3, 4$) and $\Omega \approx \omega_2$. Black curves are stable and red curves are unstable solutions.

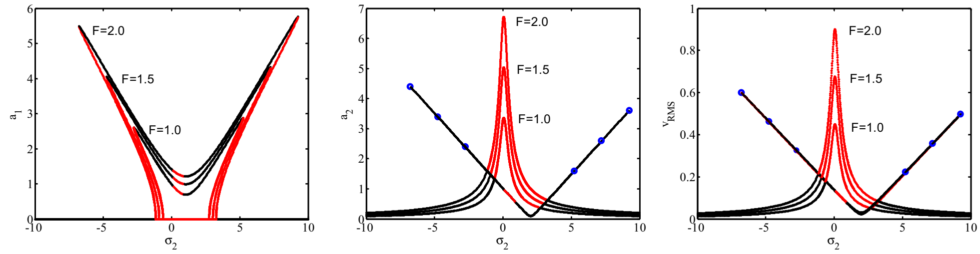

Fig. 7. Modal vibration and voltage output frequency response curves versus external detuning parameter σ_2 for different excitation levels ($F = 1.0, 1.5, 2.0$) and $\Omega \approx \omega_2$. Black curves are stable and red curves are unstable solutions. Blue circles indicate the jump points for modal vibration and voltage output amplitudes at the respective excitation levels.

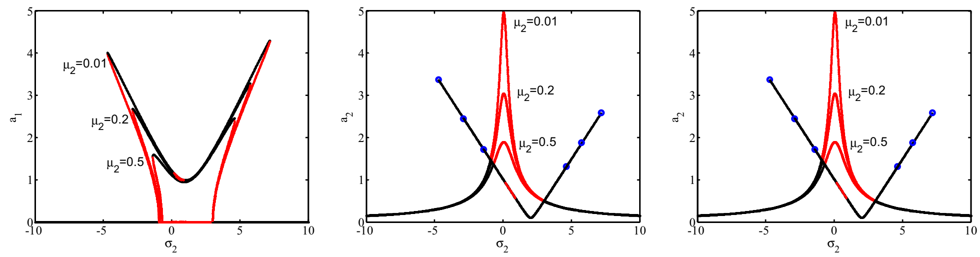

Fig. 8. Modal vibration and voltage output frequency response curves versus external detuning parameter σ_2 for different damping ratios ($\mu_2 = 0.01,\ 0.2,\ 0.5$) and $\Omega \approx \omega_2$. Black curves are stable and red curves are unstable solutions. Blue circles indicate the jump points for modal vibration and voltage output amplitudes at the respective damping ratios.

multi-valued regions the jump phenomenon occurs upward at F_2 and downward at F_1. The stability analysis of the solution branches [44] reveals the energy transfer between the vibration modes as clearly observed from the modal amplitudes.

As done in Sect. 3, vibration and voltage frequency response curves are plotted as functions of the external detuning parameter σ_2 for different values of the excitation intensity (F), linear damping ratio of mode 2 (μ_2), and load resistance-related parameter (λ). These graphs are shown in Figs. 7–9. Overall, substantial bandwidth enhancement is clearly observed for the case of $\Omega \approx \omega_2$ as well, with fundamentally different trends as compared to the first primary resonance case of $\Omega \approx \omega_1$ given in Sect. 3 (cf. Figs. 2, 4, 5).

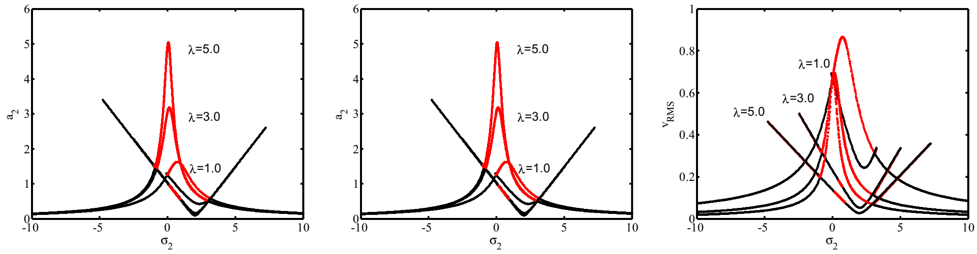

Fig. 9. Modal vibration and voltage output frequency response curves versus external detuning parameter σ_2 for different values of the reciprocal of time constant ($\lambda = 1,\ 3,\ 5$) and $\Omega \approx \omega_2$. Black curves are stable and red curves are unstable solutions.

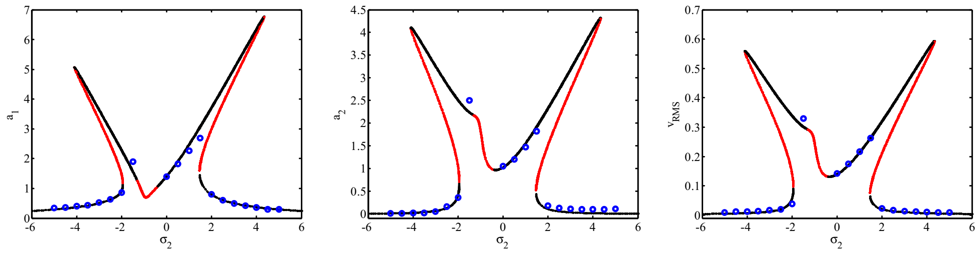

Fig. 10. Comparison of frequency-domain approximate analytical and time-domain numerical solutions for $\Omega \approx \omega_1$ ($F = 1.5$). Black curves are stable and red curves are unstable frequency-domain perturbation solutions. Blue circles are time-domain numerical solutions.

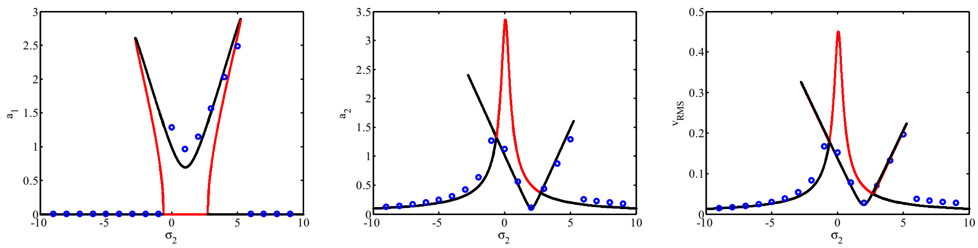

Fig. 11. Comparison of frequency-domain approximate analytical and time-domain numerical solutions for $\Omega \approx \omega_2$ ($F = 1$). Black curves are stable and red curves are unstable frequency-domain perturbation solutions. Blue circles are time-domain numerical solutions.

5 Numerical validations

Finally, in order to validate the approximate analytical solutions from the method of multiple scales, time-domain numerical simulations are obtained using the Runge-Kutta method (e.g. ode45 in MATLAB) as applied to the first-order form of the governing equations given by Eq. (1). In this section, two specific instances are chosen to compare the time-domain numerical (exact) and perturbation-based approximate analytical solutions. One case is from the first primary resonance of $\Omega \approx \omega_1$ (Fig. 2), while the other is from the second primary resonance of $\Omega \approx \omega_2$ (Fig. 7), and these comparisons are shown in Figs 10 and 11, respectively. The numerical parameters used in the perturbation and time-domain solutions are the same as those in the original Figs. 2 and 7. The blue circles in Figs. 10 and 11 represent the steady-state amplitudes of the time-domain simulation cases at the respective excitation frequencies. Very good agreement is observed between the approximate perturbation solution and the exact time domain solution, verifying the overall trends reported in the previous sections for the internal resonance-based L-shaped piezoelectric energy harvester.

6 Conclusions

In this paper, the concept of nonlinear two-to-one internal resonance was explored for broadband energy harvesting using an L-shaped beam-mass structure with quadratic nonlinearity. For this previously established 2-DOF structure (with commensurate first two linear natural frequencies, quadratic nonlinearity, and far removed higher vibration modes), linearized piezoelectric coupling and an external electrical load were introduced in order to obtain the governing electromechanical equations to simulate broadband energy harvesting performance. In the resulting electromechanical system with two-to-one internal resonance, two cases of primary resonance were reported for frequency bandwidth enhancement in energy harvesting; namely excitations near the first and the second linear natural frequencies. Significant bandwidth enhancement was reported in each case with qualitative differences especially due to the saturation phenomenon associated with the case of primary resonance excitation near the second linear natural frequency. Effects of various parameters, such as the excitation level, mechanical damping, and load resistance were also reported. Simulations based on the approximate analytical solution using the method of multiple scales were also validated against time-domain numerical simulations for specific instances. Overall, this 2-DOF configuration with quadratic nonlinearity and two-to-one internal resonance extends the bandwidth enhancement capability for 2-DOF configurations as compared exploiting two linear modes.

The authors acknowledge support from the National Natural Science Foundation of China (No. 11272016), Beijing Municipal Natural Science Foundation (No. 3122009) and Project of Beijing Municipal Commission of Education, and from the U.S. National Science Foundation grant CMMI-1254262.

References

1. S. Roundy, P.K. Wright, J. Rabaey, Computer Comm. **26**, 1131 (2003)
2. S.P. Beeby, M.J. Tudor, N. White, Meas. Sci. Technol. **17**, R175 (2006)
3. S.R. Anton, H.A. Sodano, Smart Mater. Struct. **16**, R1 (2007)
4. K. Cook-Chennault, N. Thambi, A. Sastry, Smart Mater. Struct. **17**, 043001 (2008)
5. N. Elvin, A. Erturk, *Advances in energy harvesting methods* (Springer Science & Business Media, 2013)
6. P. Glynne-Jones, et al., Sensors Actuators a-Phys. **110**, 344 (2004)
7. D.P. Arnold, IEEE Trans. Magnet. **43**, 3940 (2007)
8. S.D. Moss, et al., Smart Mater. Struct. **24**, 023001 (2015)
9. P.D. Mitcheson, et al., Sensors Actuators a-Phys. **115**, 523 (2004)
10. C.P. Le, et al., J. Int. Mat. Syst. Struct. **23**, 1409 (2012)
11. S. Roundy, P.K. Wright, Smart Mater. Struct. **13**, 1131 (2004)
12. N.E. DuToit, B.L. Wardle, AIAA J. **45**, 1126 (2007)
13. A. Erturk, D.J. Inman, Smart Mater. Struct. **18** (2009)
14. S. Adhikari, M. Friswell, D. Inman, Smart Mater. Struct. **18**, 115005 (2009)
15. L. Wang, F.G. Yuan, Smart Mater. Struct. **17** (2008)
16. A. Adly, et al., J. Appl. Phys. **107** (2010)

17. R.D. Kornbluh, et al., *From boots to buoys: promises and challenges of dielectric elastomer energy harvesting*. in *SPIE Smart Structures and Materials+Nondestructive Evaluation and Health Monitoring* (International Society for Optics and Photonics, 2011)
18. M. Aureli, et al., Smart Mater. Struct. **19**, 015003 (2010)
19. S. Anton, K. Farinholt, A. Erturk, J. Int. Mat. Syst. Struct., 1045389X14541501 (2014)
20. Q. Deng, et al., Int. J. Solids Struct. **51**, 3218 (2014)
21. A. Erturk, D.J. Inman, *Piezoelectric energy harvesting* (John Wiley & Sons, 2011)
22. L. Tang, Y. Yang, C.K. Soh, J. Intel. Mat. Syst. Struct. **21**, 1867 (2010)
23. S.P. Pellegrini, et al., J. Int. Mat. Syst. Struct., 1045389X12444940 (2012)
24. J. Twiefel, H. Westermann, J. Int. Mat. Syst. Struct. **24**, 1291 (2013)
25. R. Harne, K. Wang, Smart Mat. Struct. **22**, 023001 (2013)
26. M.F. Daqaq, et al., Appl. Mechan. Rev. **66**, 040801 (2014)
27. I.-H. Kim, et al., Appl. Phys. Lett. **98**, 214102 (2011)
28. X. Tang, L. Zuo, J. Sound Vibr. **330**, 5199 (2011)
29. O. Aldraihem, A. Baz, J. Int. Mat. Syst. Struct., 1045389X11402706 (2011)
30. A. Aladwani, et al., J. Vibr. Acoust. **134**, 031004 (2012)
31. H. Wu, et al., J. Int. Mat. Syst. Struct., 1045389X12457254 (2012)
32. B. Mann, N. Sims, J. Sound Vibr. **319**, 515 (2009)
33. R. Ramlan, et al., Nonlinear Dyn. **59**, 545 (2010)
34. D.A. Barton, S.G. Burrow, L.R. Clare, J. Vibr. Acoust. **132**, 021009 (2010)
35. A. Erturk, J. Hoffmann, D.J. Inman, Appl. Phys. Lett. **94** (2009)
36. F. Cottone, H. Vocca, L. Gammaitoni, Phys. Rev. Lett. **102**, 080601 (2009)
37. G. Litak M. Friswell, S. Adhikari, Appl. Phys. Lett. **96**, 214103 (2010)
38. A. Arrieta, et al., Appl. Phys. Lett. **97**, 104102 (2010)
39. S.D. Nguyen, E. Halvorsen, I. Paprotny, Appl. Phys. Lett. **102**, 023904-023904-4 (2013)
40. E. Halvorsen, Phys. Rev. E **87**, 042129 (2013)
41. S. Zhao, A. Erturk, Appl. Phys. Lett. **102**, 103902 (2013)
42. R. Harne, M. Thota, K. Wang, Smart Mat. Struct. **22**, 125028 (2013)
43. L. Tang, Y. Yang, Appl. Phys. Lett. **101**, 094102 (2012)
44. A. Haddow, A. Barr, D. Mook, J. Sound Vibr. **97**, 451 (1984)
45. L.-Q. Chen, W.-A. Jiang, J. Appl. Mechan. **82**, 031004 (2015)
46. A. Erturk, J.M. Renno, D.J. Inman, J. Int. Mat. Syst. Struct. **20**, 529 (2009)
47. A.H. Nayfeh, D.T. Mook, *Nonlinear Oscillations* (John Wiley & Sons, 2008)
48. S. Leadenham, A. Erturk, Smart Mat. Struct. **24**, 055021 (2015)
49. A.H. Nayfeh, D.T. Mook, L.R. Marshall, J. Hydronautics **7**, 145 (1973)
50. B. Balachandran, A. Nayfeh, Nonlinear Dyn. **2**, 77 (1991)